JLAB-PHY-97-04

Development of a small field of view scindmmmography camera: measurements and simulations.

Daniela Steinbach*, Allen Goode^, Farzin Farzanpay*, Stan Majewski*, Drew Weisenberger*, Mark B. Williams^, and Randy Wojcik*.

*Detector Group, Thomas Jefferson National Accelerator Facility, Newport News, VA 23606, ^University of Virginia, Charlottesville, VA, 22903.

ABSTRACT

We report on studies of a small field of view scintimammography camera based on a position sensitive PMT and a crystal scintillator array. A 5-inch R3292 Hamamatsu PMT was coupled to a variety of scintillators, including pixelized NaI(TI), Csi (Na) and YAP. Laboratory and phantom studies were performed to compare performances of the above scintillator sensors with special emphasis on spatial resolution and scatter rejection. The results of Monte Carlo simulations for different pixel sizes are also presented.

Keywords gamma-ray, imaging, mammography, scintimarnmography, small field of view gamma camera, application specific gamma imager, breast cancer detection, YAP, CsI(Na), NaI(TI), pixelized

1. INTRODUCTION

Routine screening mammograms are recommended for women over 40 to 50 by the American Cancer Association to identify breast cancer patients as early as possible as the patient's prognosis is better the earlier the cancer is recognized and treated. This approach leads to many cases of suspicious lesions found on screening mammograms. Core needle biopsies are often warranted, but are performed on benign lesions in about 80% of the cases. They are invasive, painful, and likely to leave scar tissue in the breast that makes future mammograms harder to read. An alternative procedure is sought to distinguish malignant from benign lesions. There is much interest in nuclear imaging of the breast as nuclear medicine is successfully used in other areas of oncology and it can offer high sensitivity and specificity for breast lesions.[1,2,3] Scintimammography might be a valuable alternative to current methods of patient diagnosis if it can be made reliable and cost effective. Current gamma cameras are not optimized for lesion detection in dm breast and the development of an application specific gamma camera might make a crucial difference in the reliability of breast scans.

After ten minutes post injection of 20 mCi of ^{99m}Tc, most of the activity is concentrated in organs like the heart (0.24 mCi) and the liver (3.4 mCi), for example. While a malignant tumor might be expected to take up 10 times more radiation per cc than the surrounding breast tissue, the total uptake in the breast might only be 0.05 mCi. A 2cc hot spot, for example, due to a malignant lesion, might be several centimeters deep in the breast and close in geometry to much stronger sources. Positioning the detector close to the breast without including the patient's organs or torso in the field of view, and rejecting scatter from the data, are crucial steps in reliable cancer detection in the breast.[4]

We present our results from imaging experiments with several small phantoms as well as with a fully tissue equivalent anthropomorphic human torso phantom in a clinical environment. Permitting organs and body cavities to be filled with appropriate tracer concentrations the phantom realistically replicates the effect of gamma attenuation and scattering. We compared the performance of cameras based on three different crystal scintillators and evaluated different geometries for phantom imaging as well as the effects of lead apron shielding.

2. EXPERIMENTAL DETAILS

2.1 Apparatus and Data Acquisition System

Our detector is based on a 5 inch Hamamatsu R3292 position sensitive photomulitipliertube (PSPMT), an array of small pixels of a scintillator, and a collimator. See Figure I for a schematic. We obtained data with YAP, NaI(TI) and

CsI(Na) arrays. The readout system used in the present study was of the type described in our previous paper [5]. We have used anode wire sectors of two or four wires each to reduce the original number of 28x and 28y individual readout channels from the PSPMT. The 10 by 10 cm square YAP matrix was made up of 3*3*10 mm^3 crystal pixels. The NaI(TI) array was the same size, but made of 3.5*3.5*6 mm^3 pixels. The CsI(Na) array had an 11 cm diameter active area to match the size of the photocathode and was made of 2.25*2.25*6 mm^3 crystal pixels. Both the NaI(TI) and the CsI(Na) imagers had 14x and 14y wire sectors coming from the PSPMT while the YAP camera operated with a simpler readout of 7x and 7y wire sectors. The anode sector signals were amplified and delayed before entering individual ADC channels. The signal from the last dynode of the PSPMT was used to generate an ADC gate. The data acquisition system was based on FERA ADCs from LeCroy and uses a Power Macintosh 8100 workstation as the host computer, running the Kmax data acquisition software from Sparrow Corporation. Determination of the position of gamma interaction in the crystal matrix was achieved by a calculation of the center of gravity of the charge distribution and the x and y anode sectors of the PSPMT.

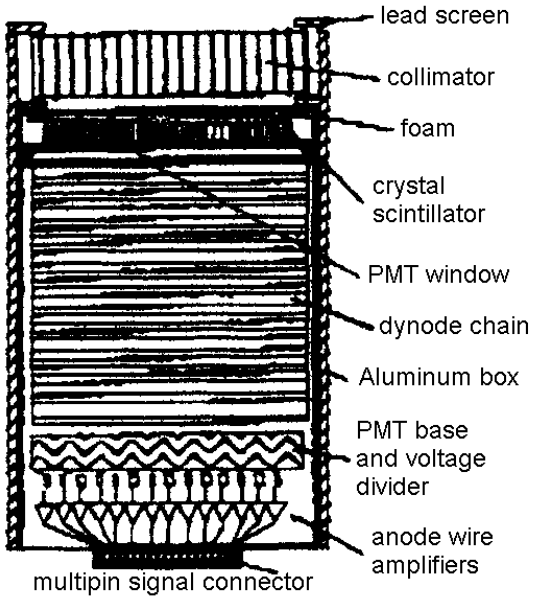

Figure 1. Schematic of the detector

Table 1. Properties of crystal scintillators used in the tested scintillator arrays.

Scintillator	NaI(TI)	CsI(Na)	YAP
Formula	NaI:TI	CsI:Na	$YAlO_3$:Ce
Rel. Light Yield	100	65-83	40
Peak Wavelength (nm)	410	420	370
Decay Constant (ns)	230	640	25
Density (g/cc)	3.67	4.51	5.37
Index of Refraction	1.85	1.79	1.95
Hygroscopic?	Yes	Slightly	No

2.2 Data Processing

The center of gravity of the signals from seven x wire sectors was obtained by the following equation:

$$\bar{X} = \frac{\sum_{n=1}^{7} X_n C_n}{\sum_{n=1}^{7} C_n} \qquad (1)$$

where: X (average) is the calculated x coordinate of one event,
X_n, is x-coordinate of the n-th wire sector.
C_n is the charge on the n-th wire sector in that direction.

A corresponding procedure was used for the calculation of the COG in the y direction. The resulting (Xaverage, Yaverage) coordinates marked an event in the 2 dimensional raw image plot such as the one shown in figure 5a. Figure 2 shows the relative signal amplitudes on seven wire actions, i.e. the relative charge distribution on the anode wire groups, in two events. It can be seen that most of the charge is collected on two to three output channels with the other channel outputs practically at zero level. Small fluctuations in the charges collected on these additional channels occur due to statistics and tube/electronics noise and can distort the COG calculation in equation (1). To keep these fluctuations from influencing COG calculations, only channels carrying charge above some fraction (f -factor) of the total charge were allowed to contribute to the COG calculation.

If no f-factor is used the image shows distortion, especially around the edges. Too large an f-factor introduces artifacts because the number of wire groups contributing to the COG calculation might be reduced to one or two in many cases and then the image contains a disproportionate number of events centered on a wire group. [5]

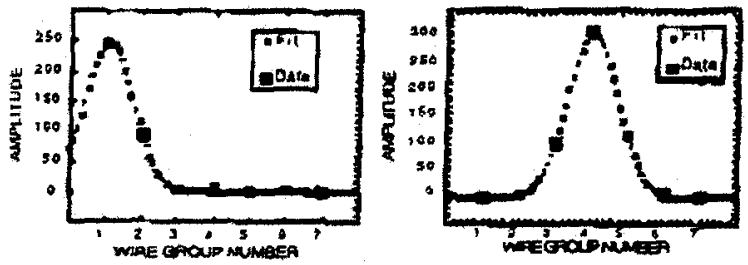

Figure 2: Distribution of signal amplitudes on wire groups along the x-axis. Each of the seven wire groups has a different amplitude for each event. Two events are shown: in the left plot the event occurred close to wire group one, in the right plot the event occurred in the center of the PSPMT.

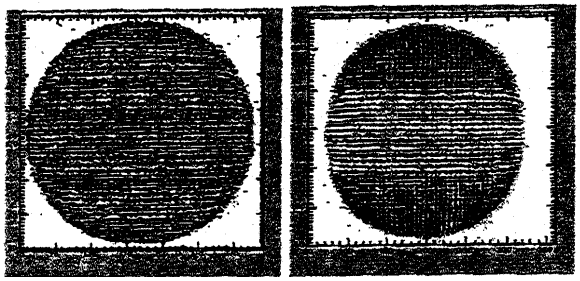

Figure 3 shows a flood image with the optimized Jefferson Lab readout with an f-factor of 0.1 compared to a flood image obtained the conventional resistive readout and algorithm.

Figure 3- Raw flood images of a 2mm pixel CsI 11 cm round crystal array obtained using (a) the improved Jefferson Lab readout and algorithm with an f-factor of 0.1 and (b) the standard resistive readout and algorithm.

2.3 Image Reconstruction

Figure 4 shows the points that have been determined to mark crystal region corners for our YAP detector. They have been obtained using a flood image. Raw images obtained from the camera (see figure 5a for example) show distorted crystal positions due to non-uniformities in the PSPMT response. Since the true relative position of each crystal is known and the crystal regions have been defined, a distortion correction is easily achieved by replotting the data identified to belong to a particular crystal into that crystal's appropriate pixel in the corrected image. An example of a raw and a corrected image is provided in figure 5.

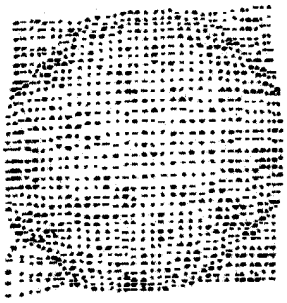

Figure 4: Map of crystal regions. Each crystal region is marked by four dots, one at each corner. 868 regions are defined in the FOV of the PSPMT, a total of 156 crystals at the four corners of the array are outside the field used for imaging.

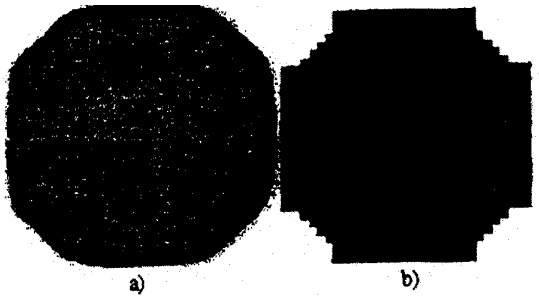

Figure 5: a)Raw image obtained from YAP camera imaging breast lesion phantom filled with ^{99m}Tc. Crystals in the region of the lesions show more counts per pixel (darker gray scale venues) than those imaging regular breast tissue of the phantom. b) In the corrected image all events are redistributed into the proper physical regions with individual energy thresholds set for each crystal.

2.4 Scatter Rejection

Figure 6 shows the uncorrected total energy spectrum of the YAP detector obtained during a flood measurement with ^{99m}Tc (140 keV), while figure 7 shows examples of energy spectra for four individual crystals. The energy spectra were obtained by summing signals from all (x and y) anode wire sectors for all events.

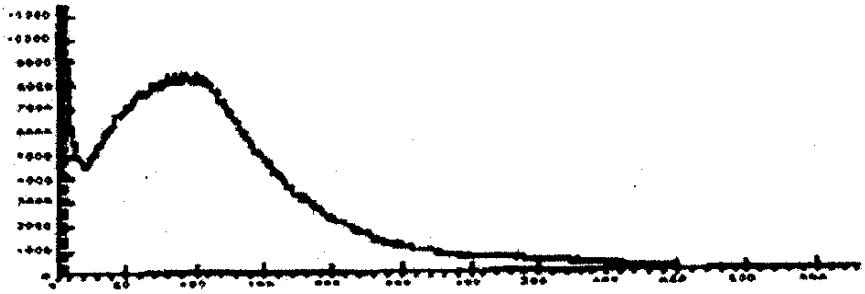

Figure 6: Total energy spectrum for ^{99m}Tc flood image.

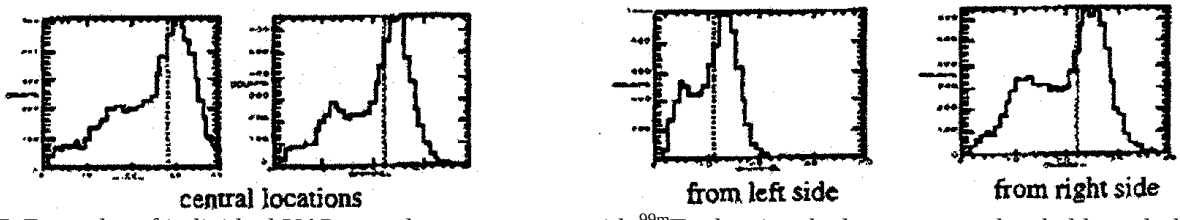

Figure 7: Examples of individual YAP crystal energy spectra with ^{99m}Tc showing the lower energy thresholds as dashed lines.

The individual energy spectra from YAP crystals-pixels have been used to set energy cut requirements on the data used to produce the corrected image. Energy thresholds were set individually at the channel indicated in each case by the dashed line at the left side of the 140 keV photopeak. Initially only events with counts above that channel would be allowed to contribute to the image. More recently we determined the peak of the individual energy spectra and center an acceptance window around the peak thus removing high energy as well as low energy background. Figure 8 shows a sample image taken with the CsI(Na) detector processed with different energy windows. The image shows a breast phantom with one lesion and a sector of a heart phantom seen at the bottom of the field of view. Too small a window limits valuable statistics but too wide a window prevents lesion demotion due to overwhelming scatter contribution.

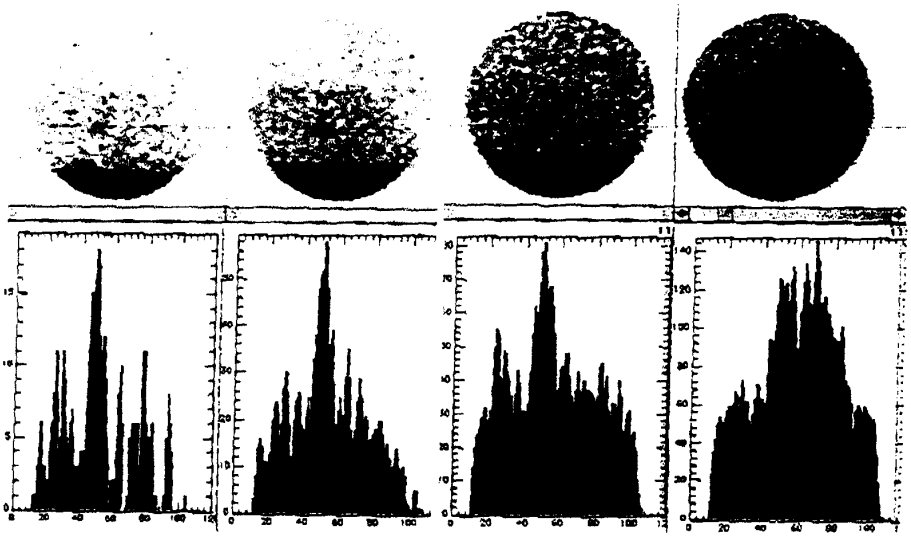
Figure 8. From left to right: the same data processed with individual energy acceptance windows of +/- 5%, 25%, 50% and 100% of the photopeak energy (channel value) and centered around the peak. If the peak sits in channel 100, for example, a 5% window would allow events that fall between channel 95 and 105 to contribute to the image. The image shows a 1.25 cc lesion with 10:1 lesion-to-breast concentration ratio.

This method of energy discrimination allowed for efficient correction of gain variations across the face of the PSPMT as well as of variations between responses from individual crystals-pixels. It treated each 3*3 mm^2 region as a pixel with its own unique energy window. A grayscale plot of the relative photopeak position in each crystal is provided in figure 9.

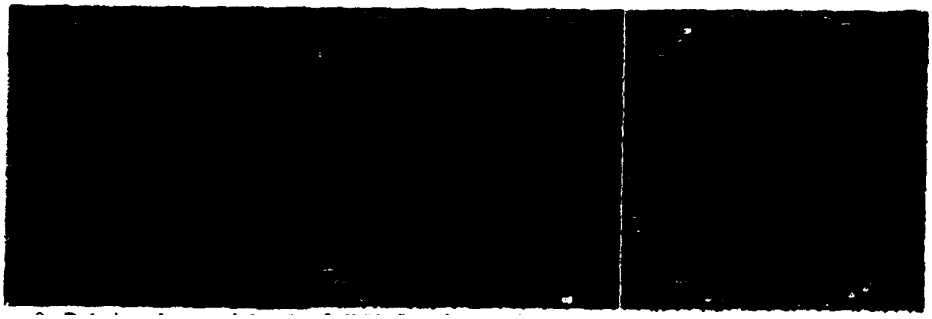

Figure 9: Relative photopeak levels of all YAP (left), NAI(TI) (middle) and CsI(Na) (right) crystals in the Field of View (FOV) of the PSPMT. The plots show position along x and y axis and photopeak position along the z axis which is represented by a gray scale. Each pixel represents one crystal and the darker the pixel the higher the gain and the center of the energy acceptance window.

The darker the area, the higher the center of the energy acceptance window. The higher photopeak positions coincided with regions of higher gain of the PSPMT as specified by the manufacturer. Figure 10a shows the peak positions for CsI(TI) crystals from crystal 1 to 2209. In part b of the same figure the histogram is expanded to show only a few rows and finally only one row of crystal cuts. As mentioned above, the corner regions of the crystal array were not used for image formation as they were not in the field of view of the PSPMT. The energy cuts for the corner regions have therefore been set to a large value (2050) beyond the dynamic range of the ADC (11 bits).

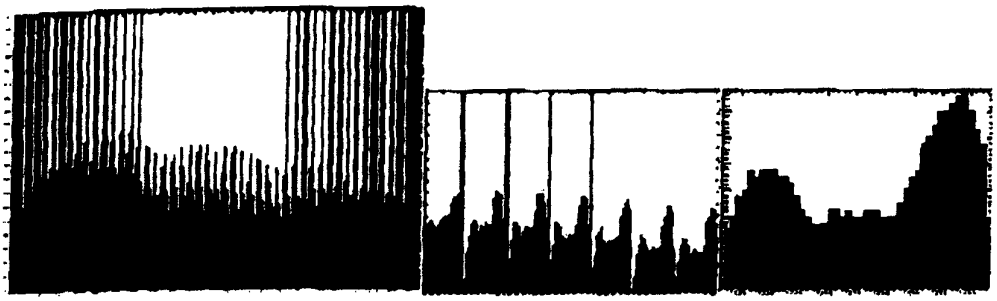

Figure 10. Peak positions for CsI(Na) crystal rows. All rows of crystals (left), a few rows of crystals (middle) (crystal 520 to 846) and one row of crystals (right) (crystal 1222 to 1269). Row one started in the lower left corner of the 2d array and contained crystal 0 to 46, row two was above that containing crystal 47 to 93, etc. The highest cuts are set for those values of an 47*47 number array that do not correspond to a crystal since our crystal array is round and measures 47 crystals across only at the diameter.

3. RESULTS

3.1 Monte Carlo Simulations

When considering the optimal size of the crystal pixel for an array one has to consider several phenomena. The smaller the pixel, that can still be separated from its neighbor, the better the detector resolution. On the other hand, gamma rays are more likely to deposit energy in more than one crystal when the pixels are very small and can not stop most of the gamma rays. In that case the energy is shared between several crystals which is counterproductive to having smaller crystals.

The effect of energy sharing between neighboring pixels was studied using two simulation programs, GRIT [6] and PTS [7]. The incident gamma ray distribution was chosen to illuminate only that part of a scintillator slab that corresponded to one crystal. Counts with their center of gravity outside the crystal pixel were attributed to sharing of gamma energy from crystal to crystal. The total number of events outside the illuminated crystal was divided by the total number of detected gamma events to yield the percent of sharing. Figure 11a shows the result of a run with GRIT for YAP and a 3mm pixel. The same data is displayed in figure 11b. About 10% of the events fall outside the illuminated pixel. Figure 11c is the plot of the sharing percentiles obtained from simulation runs with seven different crystal sizes from 0.1 mm to 10 mm pixels. The results are dependent on the source geometry. A slightly different source geometry was used in

the PTS code compared to the GRIT code. The gammas did not come in at a perfect right angle in both cases. Results from both programs are shown in figure 11c.

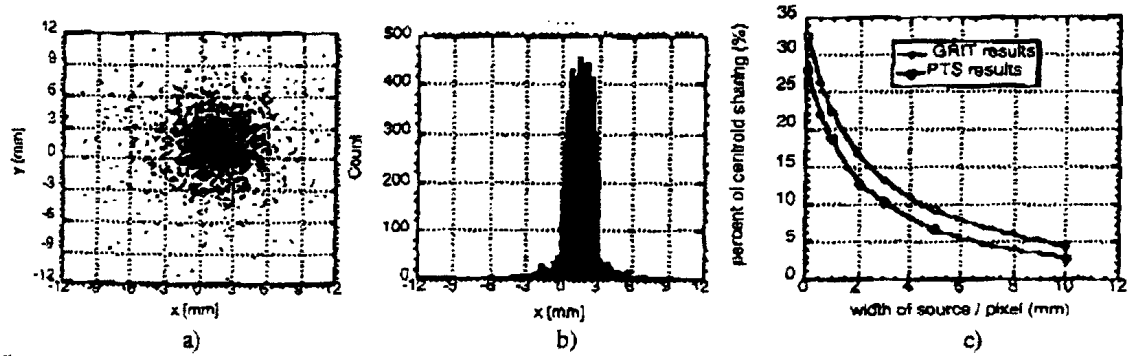

Figure 11. Crystal size versus energy sharing for YAP.

3.2 Laboratory Tests and Development of the Instrument

After initial work with a YAP array we moved to CsI and NaI arrays because these crystals have better energy resolution. The energy resolution is important for efficient scatter rejection. Figures 12, 13 and 14 show flood images of the YAP, NaI(TI), and CsI(Na) arrays described above. Darker gray scale values correspond to higher counts in the pixel. Each center row of crystals is projected to x and the projections are shown to the right of the flood image.

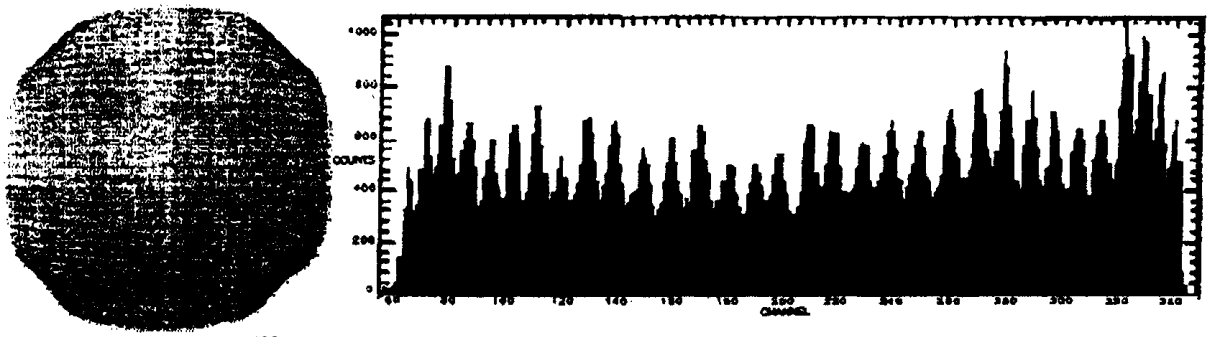

Figure 12. YAP flood. ^{106}Ru source was used to enhance the separation of crystal regions for easier calibration.

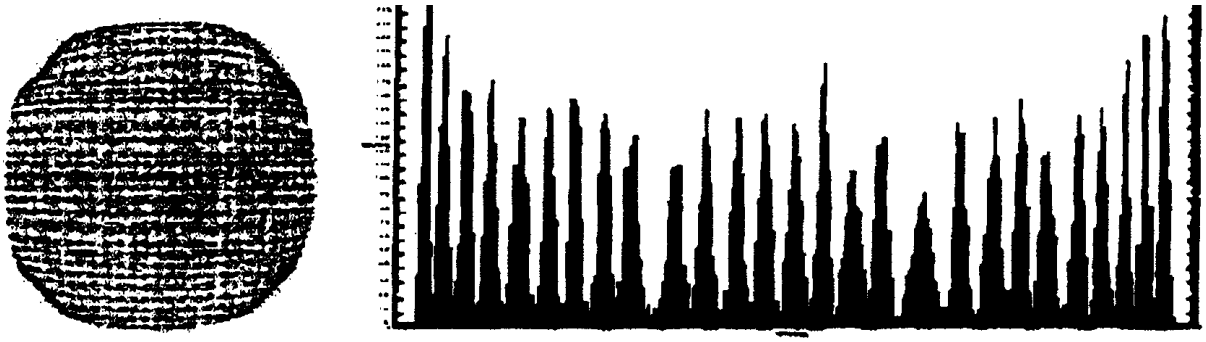

Figure 13 . NaI(TI) flood with ^{99m}Tc.

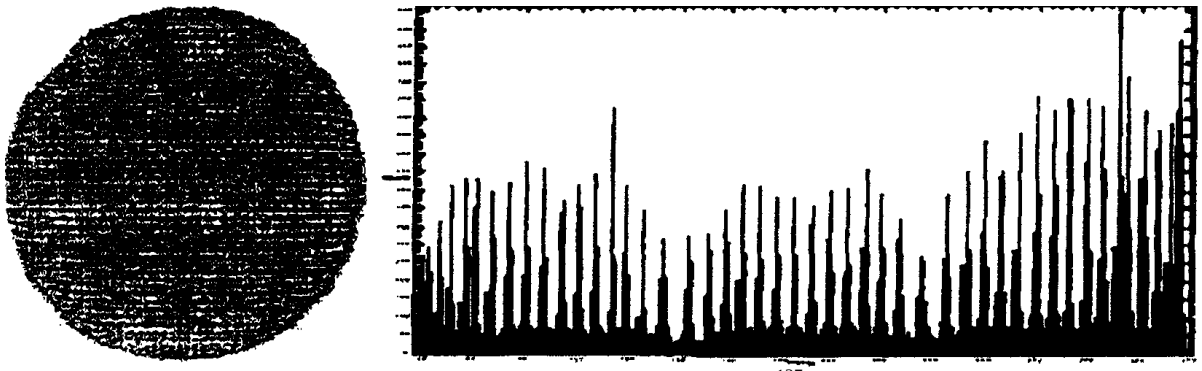

Figure 14. CsI(Na) 6mm flood with ^{137}Cs.

Energy spectra obtained from small areas of each array can be seen in figure 15. Each scintillator is used to detect 140 keV gammas from a ^{99m}Tc source. The counts in the energy spectra of 4 NaI(TI) pixels, 9 CsI(Na) pixels, and 4 YAP pixels are collected in one histogram each. The crystals subtended approximately the same area of the PSPMT in each case.

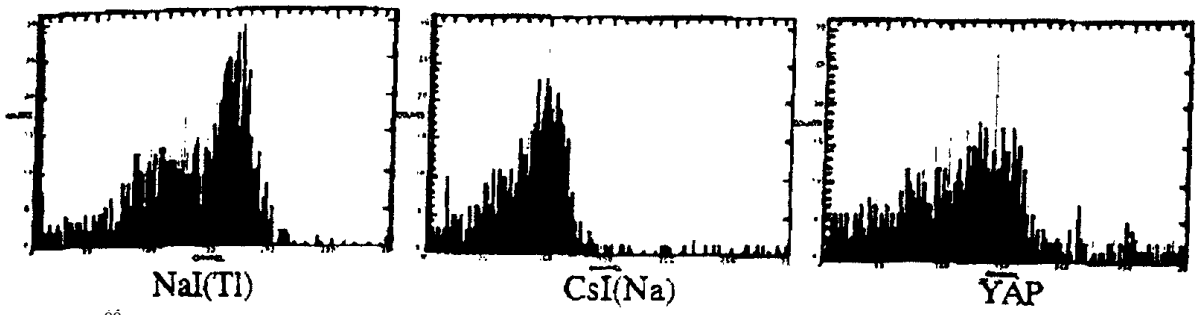

Figure 15. ^{99m}Tc energy spectra for 4 pixels of NaI(TI), 9 pixels of CsI(Na), and 4 pixels of YAP from left to right.

3.3 Detector Tests and Evaluations

After laboratory tests the detector was taken to the clinical environment. The purpose was to test and improve the detector's flexibility for positioning around the patient and to test its performance with a realistic breast cancer patient phantom before participation in clinical trials.

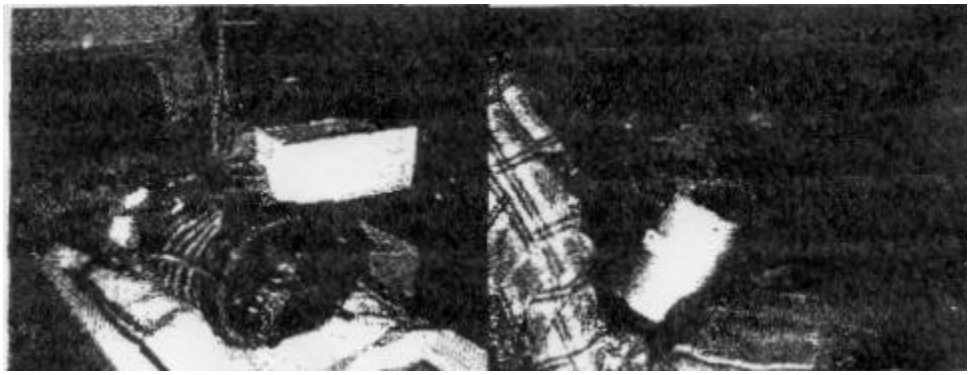

a)

Figure 16. a) The small gamma camera next to a conventional SPECT imager.

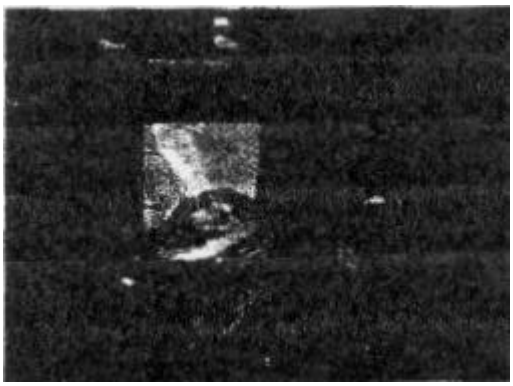

b)

Figure 16. b) The small camera used to obtain a craniocaudal view which would likely be obtained with the patient in the prone position in patient studies.

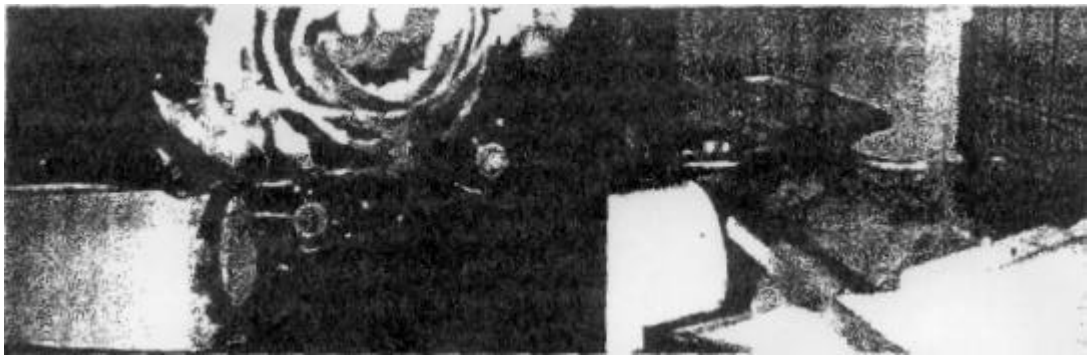

Figure 16. c) Jefferson Lab's slant hole collimator eliminates the dead area between the detector's active FOV and the chest wall of the patient in the prone position.

Figure 17 shows the results of a comparison of the CsI(Na) and NaI(TI) based detectors imaging a breast phantom under the same conditions. Likewise the performances of CsI(Na) and YAP were tested on a particular phantom set-up and the results are shown in figure 18. The torso phantom with breasts and lesions was imaged in prone and supine positions, from craniocaudal and lateral views, with and without a lead apron preventing gammas from entering the breast to produce additional scatter and gamma going into the detector. Figure 19 shows an example of the results from these studies: the right breast is imaged before and after the phantom cancer patient is outfitted with a lead apron to stop gammas originating from the heart and the liver before they enter the breast.

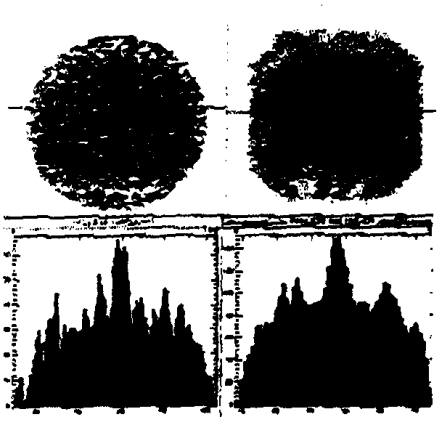

Figure 17. CsI(Na) [left] and NaI(TI) [right] detectors imaging a 500 cc breast phantom with a 2cc lesion visible. Projection lines are indicated.

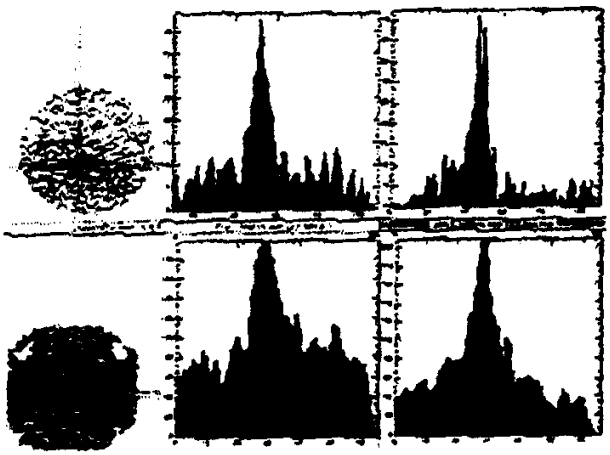

Figure 18. CsI(Na) [top row] and YAP [bottom row] based imagers under the same conditions with projections to X and to Y. 1.25 cc lesion with 10:1 lesion-to-breast ratio.

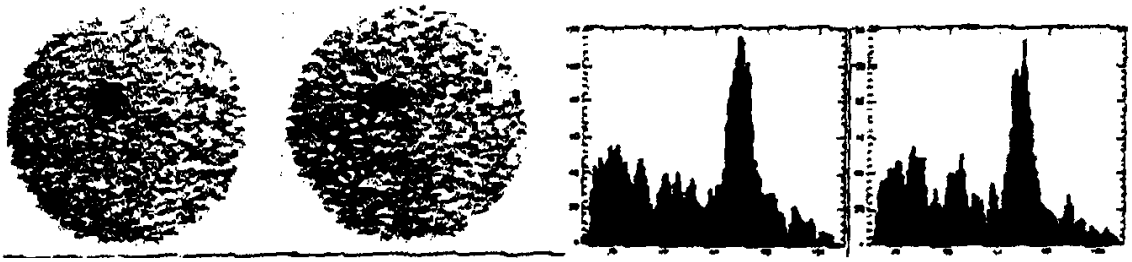

Figure 19: The phantom with breast and lesion imaged without [left] and with lead apron [right] around the torso in supine position from the right lateral view. Total counts are 17930 and 15353 in the left and right image. Projections of a slice through the lesions are made to Y for both cases. 2 cc lesion with 10:1 lesion-to-breast ratio.

4. DISCUSSION AND CONCLUSIONS

The above described tests have lead to the development of a CsI(Na) detector with 2mm pixels based on 5 inch PSPMT. The gamma imager can detect small lesions at a concentration ratio of 10: I in a realistic clinical environment. Scatter rejection with proper energy windows was found to be crucial in lesion detection.

The best results were obtained with our CsI(Na) based camera. Compared to YAP it gave better energy resolution due to higher light output. NaI(TI) has high light output but was tested with a 3mm pixel size and 10 cm square array that did not match the 1l cm round photocathode as well as our CsI(Na) array. CsI(Na) did not have a rate problem in the realistic phantom tests even though it has a long decay time. It is not hydroscopic and does not require enclosure, so that there is no window between the crystals and the PSPMT face. Such a window would spread light and worsen resolution.

ACKNOWLEDGMENTS

The authors would like to thank Dr. David Teates, Dr. Laurie Fajardo and Dr. Jayashree Parekh of UVA and Mrs. Linda Ware and Dr. Fred Dylla of Thomas Jefferson National Accelerator Facility for their strong support of the present scintimammography project. Niraj Doshi and Dr. Simon Cherry of the Crump Institute for Biological Imaging have designed and shared with us the very useful fully tissue equivalent anthropomorphic human torso phantom. They have also provided us with their estimates of realistic concentrations of radiation in different organs and shared their experience in nuclear imaging. For this we thank them very much. Tom Carstens of Jefferson Lab is thanked for his highly professional effort in the design and assembly of the amplifier boards used in the several detector prototypes developed in the course of this study. Rick Pauly, Hasmukh Shah and Burl Manis of UVA are thanked for the preparations of the many phantoms with ^{99m}Tc solution used in the evaluation tests.

REFERENCES

[1] I. Khalkhali, I. Mena, L. Diggles, "Review of imaging techniques for the diagnosis of breast cancer: a new role of prone scintimammography using, technetium-99m sestamibi", Eur J Nucl Med, vol. 21 no. 4 (1994), pp. 357-362.

[2] I. Khalkhali, I. Mena, E. Jouanne, L. Diggles. R. Venegas, J. Block, K. Alle, S. Klein, "Prone scintimammography in patients with suspicion of carcinoma of the breast", J Am Coll Surg, vol. 178(5) (1994), pp. 491-497.

[3] I. Khalkhali, J.A.Cutrone. I. G. Mena, L. E. Diggles, R. J. Venegas. H. I. Vargas, B. L .Jackson, S. Khalkhali, J. F. Moss, S. R. Klein, "Scintimammography: the complementary role of Tc-99m sestamibi prone breast imaging for the diagnosis of breast carcinomas", Radiology, vol. 196(2) (Aug1995), pp. 421-426.

[4] R. Pani. R. Pellegrini, F. Scopinaro, A. Soluri, G. De Vincentis, A. Pergolk, F. Iacopi, A. Corona, A. Grammatico, S. Fillippi, and P. L. Ballesio, "Scintillating array gamma camera for clinical use", presented at the 4th International Conference on Position-Sensitive Detectors, University of Manchester, 9- 13 September 1996.

[5] D. Steinbach, S. Majewski, M. Williams. B. Kross, A. G. Weisenberger, and R. Wojcik, Development of a Small Field of View Scintimammography Camera Based on a YAP Crystal Array and a Position Sensitive PMT, presented at the 1996 IEEE NSS, November 2-9, 1996, Anaheim, CA, also Conference Record p. 1251.

[6] Gamma Ray Interaction Tracker program released by Christian Moisan et.al. from TRIUMF and Tom Lewellen et.al. from the University of Washington in January 1997 in the new release package of DETECT_C & BUILDER. E-mail simset@u.washington.cdu for downloading instructions.

[7] Yiping Shao, Simon R. Cherry, Stefan Siegel, Robert W. Silverman, "A study of Inter-Crystal Scatter in Small Scintillator Arrays Designed for High Resolution PET Imaging", IEEE Trans. Nucl. Sci. 43(1996) pp. 1948-1944.